Analyst

ROYAL SOCIETY OF CHEMISTRY

PAPER

View Article Online
View Journal | View Issue

Cite this: *Analyst*, 2022, **147**, 4228

A handy imaging sensor array based on the phase transformation from $CsPbBr_3$ to $CsPb_2Br_5$: highly sensitive and rapid detection of water content in ethanol†

Rongmeng Gu,[a] Xiuting Li, *[b] Yan Meng, [c] Zhihui Li,[d] Hongyu Nie,[d] Xiaokun Wang[a] and Dan Xiao *[a,c,d]

Detection of the water content in ethanol has become very important in many fields; however, well-established methods usually require complex strategies and devices. Herein, a simple and non-instrument methodology was developed for the determination of the water content in ethanol. In this work, a $CsPbBr_3$@PVA imaging array sensor was constructed based on the fluorescence on/off mechanism and applied to the detection of water content for the first time. When preparing $CsPbBr_3$@PVA, the photoluminescence of $CsPbBr_3$ was quenched by water in PVA due to the decomposition of $CsPbBr_3$. By employing ethanol with fast volatilization to remove water, the decomposed composition recrystallized and formed luminescent $CsPb_2Br_5$. When the water content in ethanol was increased, the degree of the recovered fluorescence drastically reduced. To develop a portable and easily-operated methodology, the pictures of the sensor array were captured using a smartphone and quickly analyzed with ImageJ to read the gray-level values for each sample. The latter displayed a good linear relationship (R^2 = 0.995) with the water content increasing from 0% to 7% in ethanol, and a low limit of detection of 0.006% was achieved. Moreover, the sensor array showed advantages like a fast response speed (5 s), strong selectivity and application potential in real samples. This method does not require expensive spectrometers and professional personnel to operate, having the virtues of low cost, fast detection and high sensitivity.

Received 21st June 2022,
Accepted 11th August 2022

DOI: 10.1039/d2an01016j

rsc.li/analyst

Introduction

Ethanol is soluble in water at any ratio due to hydrogen bonding and similar polarity, and it is hard to avoid water in ethanol usage. However, the addition of water in some cases can bring many potential threats to the practical use of ethanol. On the one hand, ethanol is more commonly employed in organic reactions whose rates, product yields and selectivity can be negatively affected by water in ethanol.[1,2] On the other hand, ethanol is a widely used bio-fuel and abnormal water content in ethanol gasoline will result in an off-specification product, thereby increasing the rate of consumption of fuel and reducing the efficiency, even damaging vehicle engines.[3,4] Consequently, due to the efficiency and safety issues in industrial and traffic areas, the development of sensitive, accurate and facile methods to detect water content in ethanol is of great demand.

Conventional methods like the Karl Fischer method,[5] optical sensors,[6] gas chromatography (GC),[7,8] electrochemical methods,[9–11] spectrometry,[12,13] *etc.* have been commonly used for the detection of water content in ethanol, but the long testing period, the need for professional operation and the high cost of instruments greatly limit their application.[13,14] The fluorescence analysis method used for ethanol determination has some advantages of reliability and sensitivity,[15,16] but it also has inevitable disadvantages such as complex operation and poor selectivity, and the use of a fluorescence spectrometer hampers its application in speedy on-site detection. In recent years, the gray-level analysis method has been frequently reported in the sensing field. Gray-level analysis involves the RGB (three basic colors: Red, Green and Blue) model of images which can be divided into 256 levels with image analysis software for quantifying the color depth of images.[17] The color of the images taken with a smartphone

[a]*College of Chemical Engineering, Sichuan University, Chengdu 610065, China. E-mail: xiaodan@scu.edu.cn*
[b]*Institute for Advanced Study, Shenzhen University, Shenzhen 518060, China. E-mail: xiuting.li@szu.edu.cn*
[c]*Institute of New Energy and Low-Carbon Technology, Sichuan University, Chengdu 610064, China*
[d]*College of Chemistry, Sichuan University, Chengdu 610064, China*
† Electronic supplementary information (ESI) available. See DOI: https://doi.org/10.1039/d2an01016j

can be related to the analyte content *via* corresponding software; thus, a smartphone has been widely used in the sensing field for on-site applications due to its portability, easy operation, low cost and high imaging quality.[18–20] Kong *et al.* detected the water content from 20% to 55% in ethanol *via* a smartphone with the help of fluorescent Ag nanoclusters (Ag NCs); however, there are also some not so ideal results like the relatively high limit of detection (LOD = 4.48%), long response time (at least 2 minutes for incubating the probe with ethanol), and poor ability to detect low water content.[20] Therefore, considering the complexity and diversity of ethanol use scenarios, developing a sensitive, convenient and efficient method to detect water content in ethanol has the pivotal strategic significance.

In contrast to the chemical instability of organic–inorganic perovskites, all-inorganic perovskites without a volatile organic component have an excellent thermal stability owing to their chemical composition.[21] As a new type of photoelectric nanomaterial developed in recent years, all-inorganic cesium lead halide perovskite quantum dots (PQDs) $CsPbX_3$ (X = Cl, Br, I) have a narrower maximum half peak width, stronger defect tolerance structure, and higher light absorption efficiency and photoluminescence quantum yield (PLQY) than traditional quantum dots,[22–24] and hence have been applied in various electronic and optoelectronic fields, such as photoemission,[25–27] photovoltaics,[28] photodetectors[29] and photocatalysts.[30] In addition, the phase transition mechanism of this perovskite has been extensively studied. Some of the research groups reported on the transformation of $CsPbBr_3$ to a 2D $CsPb_2Br_5$ system under $PbBr_2$ rich conditions.[31–35] The phase transitions from $CsPbBr_3$ to $CsPb_2Br_5$ can be triggered by regulating the reaction temperature, time, and Pb/Cs ratio or employing water. Several reports show that $CsPb_2Br_5$ has a strong green emission.[32,36,37] Water-induced structural changes will cause great photoluminescence (PL) changes due to the high PLQY of $CsPbBr_3$ and $CsPb_2Br_5$, which can be easily captured by a smartphone and applied in the sensing field with gray-level analysis. As a result, the significant change of PL can greatly improve the sensitivity of detection, which will expand the application of perovskite materials in the field of analytical chemistry.

Herein, we physically mixed $CsPbBr_3$ QDs with unreactive polyvinyl alcohol (PVA) to prepare a membrane-based $CsPbBr_3$@PVA sensor and achieved sensitive, visual and real-time detection of the water content in ethanol by using a smartphone instead of a fluorescence spectrometer. The water in PVA will damage the structure of green fluorescent $CsPbBr_3$, causing deconstruction and fluorescence quenching of $CsPbBr_3$. After the addition of anhydrous ethanol to the fluorescence quenched $CsPbBr_3$@PVA film, the evaporation of anhydrous ethanol removed water molecules in the membrane, while the products of $CsPbBr_3$ decomposition recrystallized into green fluorescent $CsPb_2Br_5$ microplates and the recovered fluorescence could be clearly observed. As the water content in ethanol increases, the decrease in the green fluorescence intensity can be conveniently distinguished using a smartphone under a UV lamp. To develop a portative, time-saving and cost-effective detection method, small black wafers loaded with the fluorescence quenched $CsPbBr_3$@PVA are used to construct a sensor array for the determination of the water content in ethanol. A smartphone was used to quickly acquire the images of the sensor array, the color of which was then analyzed with a computer and linear regression was performed. The sensor array exhibited high sensitivity, good selectivity, a low LOD down to 0.006%, and a fast time response of only 5 s, demonstrating great potential for future implementation in the on-site monitoring of water content in ethanol.

Experimental section

Materials

All chemicals were analytical-reagent grade. Sodium hydroxide (NaOH) was purchased from Sigma-Aldrich. Polyvinyl alcohol 2488 (PVA 2488) was provided by Macklin. Formaldehyde (37%) was received from Chongqing Beibei Chemical Reagent Factory. Propyl alcohol was supplied by Chengdu Kelong Chemical Reagent Factory. Butanol was purchased from Tianjin Fuyu Fine Chemicals Co., Ltd. Methylene chloride (CH_2Cl_2) came from Adamas Beta (Shanghai) Chemical Reagent Co., Ltd. Hydrochloric acid (HCl), anhydrous ethanol (≥99.7%), acetone and methanol were from Chengdu Chron Chemicals Co., Ltd. Calcium oxide (CaO) was from Tianjin Kemiou Chemical Reagent Co., Ltd. Ultrapure water (18.2 MΩ cm, produced from a Millipore water purification unit) was used in all experiments. $CsPbBr_3$ QDs were from YangMing Quantum Technology LTD., Shenzhen 518000, China.

Instrumentation and apparatus

Fluorescence spectra (FL spectra) were measured using a Hitachi F-7000 spectrometer under an excitation wavelength of 365 nm. For analysis, the sample was spread on the glass sheet to prepare the sample membrane. The sample plate was placed in a 1 × 1 cm quartz cell. The PLQY was analyzed using an Edinburgh FLS1000 spectrophotometer with an integrated sphere by excitation at 365 nm wavelength. Time-resolved fluorescence measurements were performed on an Edinburgh FLS1000 spectrophotometer with 375nm-EPL as the single wavelength excitation light source. Fourier infrared spectra (FT-IR) were carried out using a Thermo Fisher Nicolet iS50 FT-IR spectrometer. The X-ray diffraction (XRD) patterns were recorded using the Rigaku Ultima IV diffractometer. The high resolution transmission electron microscopy (HRTEM) and transmission electron microscopy (TEM) images were recorded on a FEI Tecnai G2 F20 Field Emission Electron Microscope. X-ray photoelectron spectroscopy (XPS) was conducted on Thermo Scientific NEXSA with the X-ray source of Monochromatic AlKa source. The fluorescence images of the sensor array irradiated under an ultraviolet (UV) lamp (365 nm) were recorded by iPhone12 and grey-level analyzed using ImageJ software.

Construction of $CsPbBr_3$@PVA sensor array

Dehydrating purchased anhydrous ethanol. For achieving better detection performance, purchased anhydrous ethanol was dehydrated before using and configuring solutions. 1 g of CaO was added to 100 mL of ethanol (≥99.7%), then the solvent was distilled after refluxing for 2 h and stored in a sealed glass container that contained an activated 4 Å molecular sieve. The anhydrous ethanol with dehydrating treatment was considered as approximately 0% water content.

Preparation of PVA. 20 mL of water and 1.6 g of PVA 2488 were added to the beaker, following by heating and stirring at 90 °C until fully dissolved. When the temperature drops to 80 °C, 1 mL of formaldehyde (37%) is added and stirred at this temperature for 15 minutes. Then 500 μL of HCl (10%) was injected and polycondensation was carried out at 80 °C. After the bubbles and viscosity of the mixture rise sharply, the pH value was adjusted to 8 with NaOH immediately. Finally, water was added until the total mass of the mixture was 20 g while the mixture was stirred well.

Construction of $CsPbBr_3$@PVA sensor array. 0.06 g of $CsPbBr_3$ was mixed evenly with 1 g of PVA, the mixture was left in the dark at room temperature for 32 hours to acquire the fluorescent-quenched $CsPbBr_3$@PVA (Q $CsPbBr_3$@PVA). The $CsPbBr_3$@PVA sensor is obtained by coating 0.015 g of Q $CsPbBr_3$@PVA on a black wafer with a diameter of 1 cm. 4 μL of the liquid to be measured was slowly added to the sensor array after Q $CsPbBr_3$@PVA was naturally dried into a film, and 1 min was needed to ensure the complete response of Q $CsPbBr_3$@PVA to the liquid. Finally, the fluorescence images of the sample spots irradiated under an ultraviolet (UV) lamp (365 nm) were recorded by iPhone12 and grey-level was analysed using ImageJ software.

Results and discussion

Characterization

The $CsPbBr_3$ QDs, fluorescence-quenched $CsPbBr_3$@PVA (Q $CsPbBr_3$@PVA, the mixture of $CsPbBr_3$ and PVA for a period of time), and fluorescence-recovered $CsPbBr_3$@PVA (R $CsPbBr_3$@PVA, the product of adding ethanol to Q $CsPbBr_3$@PVA) were investigated with transmission electronic microscopy (TEM), and their typical TEM images are shown in Fig. 1A–C. $CsPbBr_3$ cube can be seen in Fig. 1A, and the particle size distribution shown in Fig. 1G indicates that the well-dispersed $CsPbBr_3$ QDs have an average diameter of 7.4 ± 1.4 nm. The cubic $CsPbBr_3$ is not observed in Fig. 1B, while there formed small particles of 3–12 nm in diameter are likely to be the degradation products of $CsPbBr_3$ under water and their aggregates. It confirms that the structural instability of PQDs in the presence of polar molecules.[21] From Fig. 1C it is clearly seen that black, two-dimensional (2D) materials appeared after the addition of anhydrous ethanol to Q $CsPbBr_3$@PVA. The phase structure, morphology and lattice spacing of $CsPbBr_3$ and $CsPbBr_3$@PVA were investigated by HRTEM (Fig. 1D–F). Fig. 1D and F show that the lattice fringes

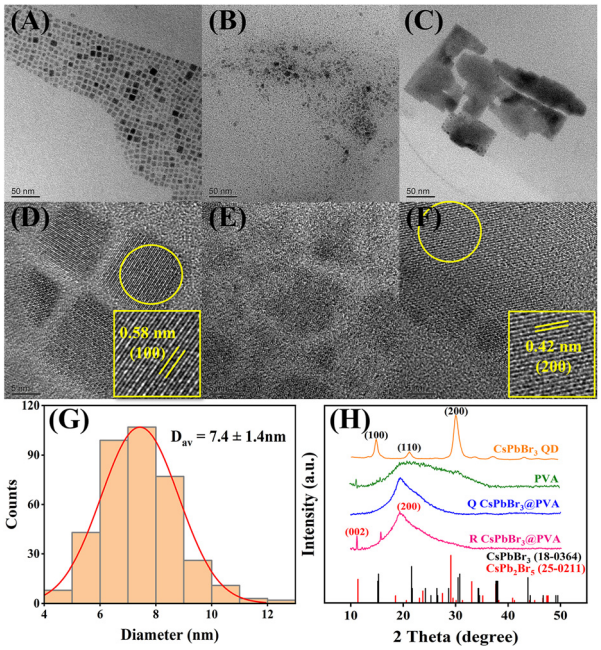

Fig. 1 TEM images of $CsPbBr_3$ QDs (A), Q $CsPbBr_3$@PVA (B), R $CsPbBr_3$@PVA (C); HRTEM images of $CsPbBr_3$ QDs (D), Q $CsPbBr_3$@PVA (E), R $CsPbBr_3$@PVA (F), enlarged HRTEM images showing lattice fringes (inset); particle size distribution of $CsPbBr_3$ QDs in (A) (G); XRD of $CsPbBr_3$ QDs (orange), PVA (green), Q $CsPbBr_3$@PVA (blue), and R $CsPbBr_3$@PVA (purple), the standard $CsPbBr_3$ (black) and $CsPb_2Br_5$ (red) obtained from the NO.18-0364 standard card, and the NO.25-0211 standard card, respectively (H).

of $CsPbBr_3$ and R $CsPbBr_3$@PVA, while Fig. 1E shows no obvious lattice fringes. The lattice space of the cube in Fig. 1D is around 0.58 nm, which results from the (100) facet of orthorhombic $CsPbBr_3$ and is in agreement with the literature.[38,39] In contrast, the spacing of R $CsPbBr_3$@PVA in Fig. 1F is about 0.42 nm; this is likely the lattice spacing from the (200) facet of $CsPb_2Br_5$, demonstrating that there probably formed new crystalline $CsPb_2Br_5$ in R $CsPbBr_3$@PVA.

To further obtain more structural information, XRD analysis of PVA, $CsPbBr_3$, Q $CsPbBr_3$@PVA, R $CsPbBr_3$@PVA and freshly prepared $CsPbBr_3$@PVA (F $CsPbBr_3$@PVA, the freshly mixture of $CsPbBr_3$ and PVA) were conducted, and the results are presented in Fig. 1H and Fig. S1.† It can be seen that the diffraction pattern of $CsPbBr_3$ QDs shows the typical lines of the orthorhombic $CsPbBr_3$ (PDF card #18-0364), indicating the successful synthesis of the $CsPbBr_3$ perovskite.[39] No other phases were observed, suggesting the high purity of the samples. The diffraction pattern of F $CsPbBr_3$@PVA in Fig. S1† kept the typical lines of $CsPbBr_3$ (the lattice planes 100, 110 and 200), indicating the crystal structure of $CsPbBr_3$ still existed when $CsPbBr_3$ and PVA mixed shortly. On the contrary, Q $CsPbBr_3$@PVA in Fig. 1H did not have the characteristic diffraction peak of $CsPbBr_3$ but only the wide diffraction peak of PVA after mixing $CsPbBr_3$ and PVA for a period of time, which can further prove the decomposition of $CsPbBr_3$. Moreover, the diffraction peaks at 11.7°, 20.9° of R

$CsPbBr_3$@PVA are respectively assigned to the lattice planes of (002), (200) of $CsPb_2Br_5$ (PDF card #25-0211), which is consistent with lattice spacing in Fig. 1F and further confirms the formation of $CsPb_2Br_5$ crystals in R $CsPbBr_3$@PVA.[31] From Fig. 1C, the $CsPb_2Br_5$ nanosheets do not show an uniform thickness, which may be due to the migration and overlap of recrystallized $CsPb_2Br_5$ given the rapid spread and volatilization of anhydrous ethanol in Q $CsPbBr_3$@PVA.

XPS characterization tests of F $CsPbBr_3$@PVA and R $CsPbBr_3$@PVA can also prove the structure transformation process from $CsPbBr_3$ to $CsPb_2Br_5$ in $CsPbBr_3$@PVA. The survey spectrum (Fig. 2) shows that Cs, Pb, and Br are the main elements in F $CsPbBr_3$@PVA and R $CsPbBr_3$@PVA samples, and the identifiable impurity of C is attributed to the PVA. From the statistics result (Table 1), the atomic proportion for Cs, Pb, and Br was 0.8%, 1.18%, 2.87% for F $CsPbBr_3$@PVA, respectively, close to the stoichiometry ratio of $CsPbBr_3$. While the atomic proportion for Cs, Pb, Br was 1.07%, 1.55%, 4.59% for R $CsPbBr_3$@PVA, respectively, close to the stoichiometry ratio of $CsPb_2Br_5$. The element composition and stoichiometry ratio of F $CsPbBr_3$@PVA and R $CsPbBr_3$@PVA samples examined by XPS were further confirmed the structure transformation process from $CsPbBr_3$ to $CsPb_2Br_5$.

Furthermore, the PVA, R $CsPbBr_3$@PVA, Q $CsPbBr_3$@PVA and F $CsPbBr_3$@PVA were studied with a FL spectrophotometer to clarify the effect of water and anhydrous ethanol on the fluorescence intensity of $CsPbBr_3$@PVA. The FL spectra shows the maximum PL peaks at 515 nm for F $CsPbBr_3$@PVA and 517 nm for R $CsPbBr_3$@PVA while no emission peak for Q $CsPbBr_3$@PVA, which demonstrates that water quenches the fluorescence of $CsPbBr_3$ and anhydrous ethanol triggers the recovery of the fluorescence (Fig. 3A). The PLQY, defined as the percentage of photons emitted over photons absorbed by the sample, was determined by using an integrating sphere. A direct measurement was performed to measure PLQY of F $CsPbBr_3$@PVA and R $CsPbBr_3$@PVA. Emission spectra measured using a fluorescence photometer with an integrating sphere attachment are provided in Fig. S2.† The PLQY of 23.4% and 21.96% was observed from the solid films of F $CsPbBr_3$@PVA and R $CsPbBr_3$@PVA with the excitation wavelength of 365 nm. In addition, the time-resolved PL measurement was carried out on the F $CsPbBr_3$@PVA and R $CsPbBr_3$@PVA films to characterize carrier recombination dynamics. Fig. 3B displays that the analysis by using a biexponential fit gave an average lifetime of 8.42 ns for F $CsPbBr_3$@PVA and 230 ns for R $CsPbBr_3$@PVA. All the decay curves were fitted with a biexponential function: $I = A_1 \times \exp(t/t_1) + A_2 \times \exp(t/t_2)$, where $I = y - y_0$, $t = x$, A_1 and A_2 are weighted coefficients, t_1 and t_2 represent respectively the decay time of the fast and slow components of PL. The related coefficients of the double exponential function are listed in Table S1.† The average lifetimes were evaluated by the following formula: $\tau_{av} = (A_1 \times t_1^2 + A_2 \times t_2^2)/(A_1 \times t_1 + A_2 \times t_2)$. By using PLQY and average lifetime with the basic equations ($k_r = \Phi/\tau_{av}$ and $k_{nr} = (1 - \Phi)/\tau_{av}$, where Φ is the PLQY, and τ_{av} is the average PL lifetime), it can be estimated the radiative (k_r) decay rate of 0.000955 ns^{-1} and nonradiative (k_{nr}) decay rates of 0.00339 ns^{-1} for R $CsPbBr_3$@PVA while k_r decay rates of 0.0278 ns^{-1} and k_{nr} decay rates of 0.091 ns^{-1} for F $CsPbBr_3$@PVA. There is obvious difference in luminescence lifetimes and dynamics between F $CsPbBr_3$@PVA and R $CsPbBr_3$@PVA. As is well-established, the surface defects of $CsPbBr_3$ can easily result from reorientation or decomposition of crystal struc-

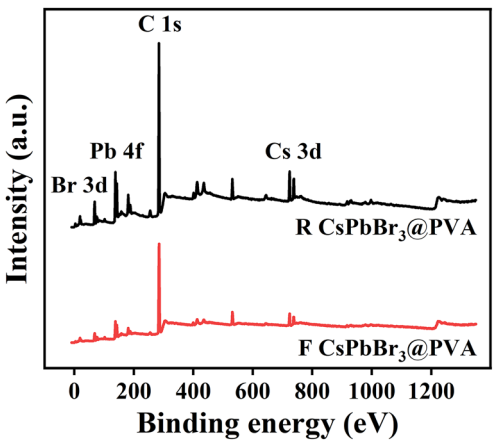

Fig. 2 XPS survey spectra of F $CsPbBr_3$@PVA and R $CsPbBr_3$@PVA.

Table 1 Specific statistics of the XPS survey for F $CsPbBr_3$@PVA and R $CsPbBr_3$@PVA

Material	Name	Peak BE	Height CPS	Area (P) CPS.eV	Atomic %
F $CsPbBr_3$@PVA	Cs 3d	723.67	9872.36	27530.86	0.8
	Pb 4f	137.78	14640.17	42454.82	1.18
	Br 3d	67.79	4528.86	8709.9	2.87
R $CsPbBr_3$@PVA	Cs 3d	723.63	23736.2	62307.01	1.07
	Pb 4f	137.68	35748.27	93946.35	1.55
	Br 3d	67.72	12089.05	23550.85	4.59

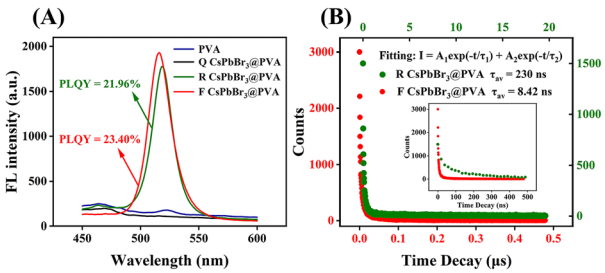

Fig. 3 FL spectra of PVA (blue), Q $CsPbBr_3$@PVA (black), R $CsPbBr_3$@PVA (green), F $CsPbBr_3$@PVA (red), red font and green font show the PLQY of F $CsPbBr_3$@PVA, and R $CsPbBr_3$@PVA, respectively (A); fluorescence decay curves of F $CsPbBr_3$@PVA (red) and R $CsPbBr_3$@PVA (green) (B). Red font and green font are axes of F $CsPbBr_3$@PVA and R $CsPbBr_3$@PVA respectively, whose decay curves are compared in the same coordinate axis within 0–500 ns (inset).

tures caused by oxygen or water. On the contrary, two-dimensional (2D) perovskite $CsPb_2Br_5$ appeared to be more resistant to ambient humidity.[40] On the one hand, moisture will greatly affect the stability of $CsPbBr_3$, so we speculate that the low fluorescence lifetime of F $CsPbBr_3$@PVA (τ_{av} = 8.42 ns) is caused by the dynamic quenching process between $CsPbBr_3$ and water in PVA.[41] On the other hand, $CsPb_2Br_5$ also showed longer fluorescence lifetime than $CsPbBr_3$ in past studies due to their difference in forceful interfacial interactions and radiative channels.[31] In addition, for $CsPb_2Br_5$, the contribution of polymer PVA to increasing carrier lifetime cannot be ignored because of its high efficiency in charge separation.[42,43] Detailed structural analysis on $CsPb_2Br_5$ will be the subject of our future work.

Principle for the detection of water content in ethanol

In this work, $CsPbBr_3$@PVA underwent a fluorescence quenching and recovery process under the induction of water and ethanol, as illustrated in Fig. 4. For the phase of gradual quenching of fluorescence from F $CsPbBr_3$@PVA to Q $CsPbBr_3$@PVA, there was a structural change due to moisture in $CsPbBr_3$@PVA induced decomposition of $CsPbBr_3$ QDs, leading to quenching of fluorescence. According to the literature, $CsPbBr_3$ has chemical instability against polar solvents like water because of the strong ionic nature of cesium lead halide perovskites.[32,44] PVA provides a medium for the contact between oil-soluble $CsPbBr_3$ QDs and water, $CsPbBr_3$ QDs can be dispersed in PVA solution to obtain $CsPbBr_3$@PVA because the polar monomer acrylate acts as one of the capping ligands of $CsPbBr_3$ QDs and the hydrophilicity of PVA can be regulated by acetal reaction with formaldehyde. The large amount of water in $CsPbBr_3$@PVA (the mass fraction of water in $CsPbBr_3$@PVA ≈ 87%) can extract CsBr from the $CsPbBr_3$ phase because of the high solubility of CsBr in water and the strong ionic nature of the $CsPbBr_3$ compound.[32,33] Thus, the PL performances of $CsPbBr_3$@PVA degraded extensively with the extension of mixing time of $CsPbBr_3$ and PVA, as shown in Fig. S3.†[45]

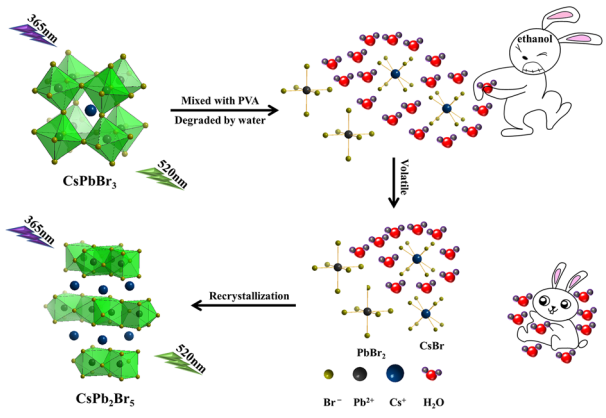

Fig. 4 Principle of phase transformation from $CsPbBr_3$ to $CsPb_2Br_5$.

For the fluorescence recovery process from Q $CsPbBr_3$@PVA to R $CsPbBr_3$@PVA, more volatile anhydrous ethanol was employed to recrystallize the Q $CsPbBr_3$@PVA to obtain R $CsPbBr_3$@PVA with PL recovered. The latter shows a similar 2D-shaped microsheet morphology (Fig. 1C) of $CsPb_2Br_5$ with the literature.[31,46] Some of the research groups reported on the transformation of $CsPbBr_3$ to 2D $CsPb_2Br_5$ system under $PbBr_2$ rich conditions. By regulating the reaction temperature, time, and Pb/Cs ratios or employing water to transform $CsPbBr_3$ to 2D perovskite-related $CsPb_2Br_5$, which required long time or heating. Here, we recrystallized $CsPb_2Br_5$ by "drying" the water with volatile ethanol. Accordingly, a part of CsBr supersaturated and precipitated out due to the escape of water in the film, and participated in the recrystallization of green fluorescent $CsPb_2Br_5$ with the insoluble PbBr, which is a thermodynamically favorable state.[32] Of course, an in-depth study of the degradation products of $CsPbBr_3$ and the recrystallization process of $CsPb_2Br_5$ will be our future research direction.

The evaporation of water molecules was monitored by measuring infrared spectroscopy of the samples before and after anhydrous ethanol treatment. As shown in Fig. S4,† the broad OH stretching vibration of the water and PVA molecules around 3300 cm^{-1} weakening after adding anhydrous ethanol. In addition, in order to prove the positive effect of water removal on the recrystallization of $CsPb_2Br_5$, the Q $CsPbBr_3$@PVA film was heated at 100 °C for 1 h to evaporate water molecules, and the recovery of green fluorescence was also observed (Fig. S5†). The fluorescence of ethanol-treated Q $CsPbBr_3$@PVA can be regenerated within a few seconds, indicating that the volatilization process accelerated by ethanol leads to the quick recrystallization and hence the recovery of green fluorescence. However, due to the large amount of hydrogen bond between water molecules and hydroxyl groups in PVA as well as the limited ability of ethanol to volatilize water, solvated CsBr always exists because water molecules cannot be completely removed, leading to the phase transition from $CsPbBr_3$ to $CsPb_2Br_5$.

Thus, the fluorescence on/off mechanism of $CsPbBr_3$@PVA can be proposed according to the above discussion, that is, $CsPbBr_3$ decomposed when being mixed with PVA which has water residue, leading to the quenching of fluorescence. When anhydrous ethanol was dropped directly on the Q $CsPbBr_3$@PVA film and volatilized partial water, the decomposed products recrystallized to form $CsPb_2Br_5$, and green fluorescence reappeared. Based on the fluorescence on/off mechanism, a facile sensor for the detection of water content in ethanol was fabricated, as shown in Fig. 5. In brief, 0.015 g of Q $CsPbBr_3$@PVA was loaded on a black wafer and formed a film with a diameter of about 1 cm. When 4 μL of ethanol solution was added to the film, $CsPb_2Br_5$ was formed and hence fluorescence light-up significantly occurred whose intensity is related to the amount of water in ethanol (Fig. 5A). The fluorescence with a high quantum yield (21.96%) from $CsPb_2Br_5$ is strong enough to be recorded by a smartphone instead of a spectrometer. Therefore, the fluorescence images of the sensor irradiated under a UV lamp (365 nm) was next recorded by a

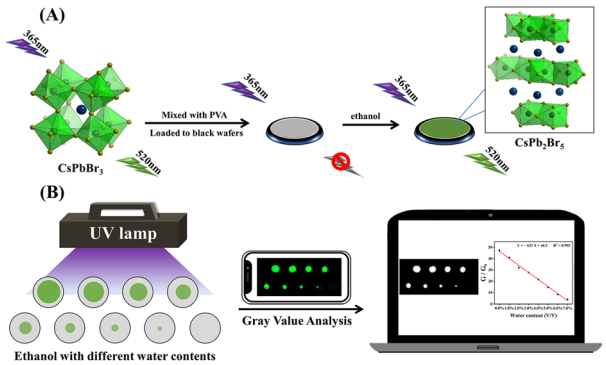

Fig. 5 Schematic illustration for the fluorescence on/off mechanism of $CsPbBr_3$@PVA (A) and the determination of water content in ethanol with $CsPbBr_3$@PVA sensor array (B).

smartphone and then grey-level analyzed using ImageJ software (Fig. 5B). Taking advantage of the digital analysis, the present strategy was further employed to quickly identify the water content of ethanol.

Rapid response to anhydrous ethanol

The entire response process of dropping anhydrous ethanol to $CsPbBr_3$@PVA sensor array was filmed with a smartphone. Video images were captured every second and the time before dropping anhydrous ethanol was defined as 0 s. Fig. 6B shows that the green fluorescence of $CsPbBr_3$@PVA began to recover within 1 s after adding anhydrous ethanol and the fluorescence intensity tends to be stable after 5 s. ImageJ was then used to analyze the gray-level values at these moments and the results are shown in Fig. 6A. From the plot of gray level ratio against time, it was found that the gray-level value of $CsPbBr_3$@PVA no longer increased significantly from 5 s. The corresponding gray-level image and three-dimensional (3D) distribution graph of gray-level values are shown in Fig. S6.† This indicates that the $CsPbBr_3$@PVA sensor array can reach the maximum response to anhydrous ethanol after 5 s. Therefore, the $CsPbBr_3$@PVA sensor array based on gray-level analysis method has the advantage of rapid response, which is essential for practical applications.

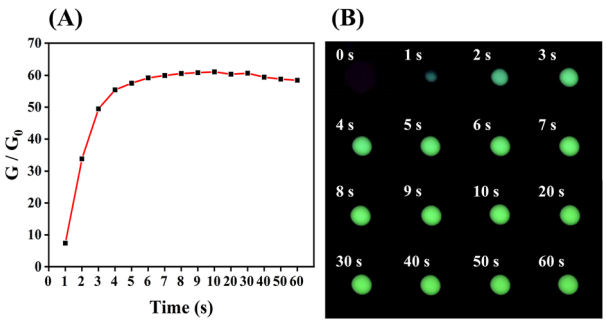

Fig. 6 The gray-level ratio (G/G_0) of $CsPbBr_3$@PVA sensor array against time after anhydrous ethanol was dropped on the film surface, where G_0 is the gray-level value before anhydrous ethanol was added (t = 0 s) (A); fluorescence image of $CsPbBr_3$@PVA sensor array at different times after dropping anhydrous ethanol (B).

Water analysis in ethanol with $CsPbBr_3$@PVA

For the best sensing performance of the proposed detection system, several experimental conditions, such as $CsPbBr_3$ concentration, mixing time and volume of anhydrous ethanol have been optimized. As shown in Fig. S7A,† the 6% $CsPbBr_3$ in PVA reached the maximum signal-to-background ratios (G/G_0). In addition, the effect of mixing time of $CsPbBr_3$ and PVA was investigated (Fig. S7B†). The maximum G/G_0 was achieved at the mixing time of 32 h. The amount of anhydrous ethanol was explored that the maximum response was achieved when 4 μL of anhydrous ethanol was dropped onto the sensor (Fig. S7C†). For more details about optimized conditions see Fig. S7 in the ESI.† The above optimization conditions were used in subsequent experiments.

Ethanol solution with different water contents was then dropped to the sensor array, and the fluorescence image of the array was recorded by a smartphone. As illustrated in Fig. 7A, with the increase of water content in ethanol from 0 to 7%, the fluorescence image (top) showed that the restored fluorescence intensity of $CsPbBr_3$@PVA greatly reduced. The gray-level analysis method was used to further study the sensor performance, and the fluorescence image was split into R (red), G (green) and B (blue) channels to quantify gray-level values of different colors with ImageJ. Fig. 7A (below) and Fig. 7C dis-

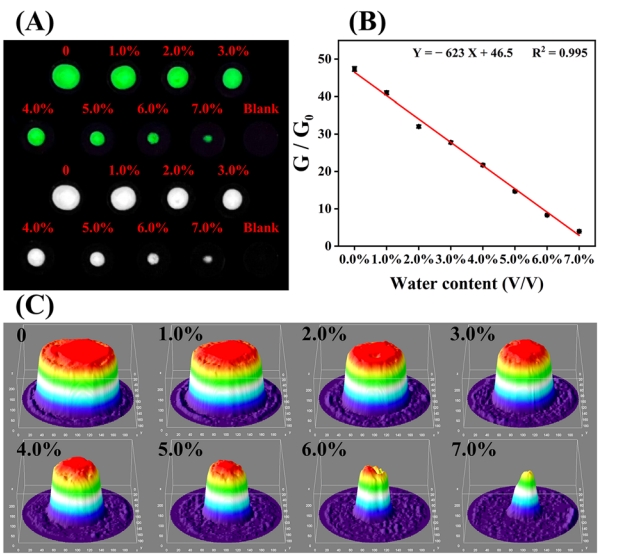

Fig. 7 Fluorescence image (top) of the $CsPbBr_3$@PVA sensor array treated with ethanol solutions with different water content and gray-level image converted from fluorescence image by ImageJ (bottom) (A); the linear fitting relationship between the gray ratio G/G_0 of the sensor and the water contents in ethanol, where G_0 is the gray-level value of the sensor without ethanol treatment (B); the corresponding 3D distribution graph of gray-level values of sensors treated with ethanol solutions with different water content (C).

played the gray-level image and 3D distribution graph of gray-level values from the G channel, respectively. The height of each coordinate point in the 3D distribution graph corresponds to the gray-level value of each point of the sensor array, so the volume of each peak reflects the total gray-level value of each wafer. With the increase of the water content, the volume of the gray-level peak also decreases correspondingly, indicating that the gray-level value of sensor array decreases gradually. This is because the volatile ability of ethanol to the water in $CsPbBr_3$@PVA is inversely proportional to the water content in the ethanol solution, and less $CsPb_2Br_5$ formed. It is difficult to form $CsPb_2Br_5$ by adding ethanol when the water content of ethanol is more than 7%. Moreover, it should be noted from the 3D distribution graph that the gray-level values of each wafer shows a trend of decreasing from the center to the edge. This can be attributed to the rapid recrystallization process results in a decrease in the concentration of ethanol while ethanol diffusing from the center to the edge of the $CsPbBr_3$@PVA film, leading to the differentiation of the production of $CsPb_2Br_5$ at different sites. In addition, the gray-level images and 3D distribution graphs of gray-level values from R and B channels are shown in Fig. S8.† The gray-level values of R, G and B varying with different water contents are displayed in Fig. S9.† It could be seen that G values decreased significantly with the increase of water content while the R and B values stayed constant. Therefore, our array sensor shows excellent sensitivity in water content detection through the gray-level analysis of the G channel. The gray value ratio (G/G_0: sample/blank) against the water content from 0% to 7% in ethanol is displayed in Fig. 7B. There was a good linear relationship which can be expressed as $y = -623x + 46.5$ (R^2 = 0.995) with the low LOD of 0.006%. Besides, different brands and models of smartphones had little effect on the results (see Fig. S10†).

Furthermore, the fluorescence sensing was recorded by a fluorescence spectrometer and the advantages of gray-level analysis method were further confirmed. A similar conclusion has also been made using the corresponding fluorescent signals recorded by the spectrometer. The results in Fig. 8 showed that F/F_0 had a good linear correlation with the water content from 0% to 6%. The linear relationship was $y = -175.9x + 12.15$ (R^2 = 0.975), and the LOD is 0.18%. However, as the measurement results of solid fluorescence are greatly affected by the surface conditions of the sample, the fluorescence intensity will change greatly with slightly different surface conditions. Thus, the linear correlation coefficient, detection range and LOD of the fluorescence analysis method are worse than those of gray-level analysis method. Moreover, the use of the fluorescence analyzer is not conducive to employ the sensor in on-site detection, which increases the cost of detection.

In brief, the sensor array has the advantages of high sensitivity, low detection limit, simple operation, low cost, and no need for complex and expensive fluorescence spectrum analyzer. The convenient and accurate on-site detection of the water content in ethanol is easily achieved within only 5 min of analysis. What's more, the sensor array can be preserved for at least 1 week with stable fluorescence recovery ability (see Fig. S11†). Compared with other reported determination methods on the water content in ethanol,[20,47–53] the $CsPbBr_3$@PVA sensor array in this work has lower LOD, better slope and faster response time, as listed in Table 2.

Specific response to ethanol

The detection specificity is one of the important factors for sensing. In order to investigate the specificity of $CsPbBr_3$@PVA sensor array to anhydrous ethanol, the response performance of the sensor to organic solvents methanol, n-propanol, n-butanol, acetone and dichloromethane was studied under the same experimental conditions. In contrast to the significant increase in fluorescence for anhydrous ethanol treatment, no clear fluorescence light-up was observed for the sensor treated with the other solvents. The corresponding grey ratios are recorded in Fig. 9. This may be because the polarities of *n*-propanol, *n*-butanol, acetone and dichloromethane are all smaller than ethanol and water. Methanol, which has a higher polarity than ethanol, is unable to expose the solvated CsBr to

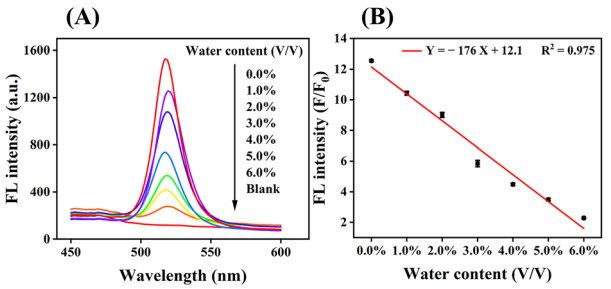

Fig. 8 FL spectra of $CsPbBr_3$@PVA with ethanol treatment (from top to bottom: 0%, 1%, 2%, 3%, 4%, 5%, 6% water content in ethanol and blank) (A); the linear fitting relationship between the FL intensity ratio F/F_0 of $CsPbBr_3$@PVA and the water contents in ethanol, where F_0 is the FL intensity of $CsPbBr_3$@PVA without ethanol treatment (B).

Table 2 Some reported methods for the determination of water content in ethanol

Method	Linear range (vol%)	Linear slope	LOD	Response time
Gray-level analysis[20]	22–55	−0.01932	4.48	1 min
Fluorescence[47]	0.05–4	None	0.03	None
Fluorescence[48]	0.5–25	0.105	0.26	None
Fluorescence[49]	10–60	0.0193	0.36	None
Fluorescence[50]	0–1	363.8	0.006	1 s
Fluorescence[51]	0–10	−6.683	0.0097	90 s
Capacitive sensing[52]	5–40	None	None	None
Thermal approach[53]	0–1 (w/w)	None	0.35	None
Fluorescence in this work	0–6	−176	0.18	None
Gray-level analysis in this work	0–7	−623	0.006	5 s

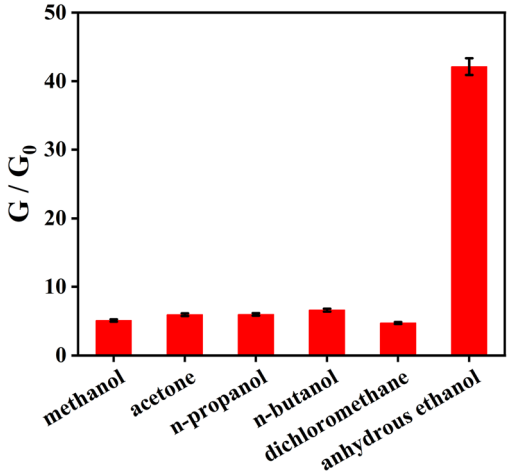

Fig. 9 Specific response of $CsPbBr_3$@PVA to anhydrous ethanol.

participate in the recrystallization process of $CsPb_2Br_5$ due to its lower boiling point and faster volatilization speed. This result proves that the sensor array has a very high selective response to anhydrous ethanol, which underpins the successful determination of the water content in ethanol and could be expanded to detect the other solvents with different polarities and volatilities mixed with ethanol.

Real sample assays

To check the practical application of $CsPbBr_3$@PVA sensor array for sensing water content in ethanol, three kinds of 95% ethanol samples from different manufacturers were selected as real samples for detection. They are from Hebei Ruikang Pharmaceutical Technology Co., LTD. (Sample 1), Nanyang Ruilikang Biological Technology Co., LTD. (Sample 2), and Shandong Anjie High-tech Disinfection Technology Co., LTD. (Sample 3). These samples labeled 5.0% of moisture content were separately dropped onto the sensor to determine the moisture content through gray-level analysis. As shown in Table 3, good recovery values (95.8% to 104%) with the relative standard deviation (RSD) ranging from 2.7% to 3.7% were obtained. The errors are within the acceptable range. These recovery results indicate that our sensor array has potential applicability to detect water content in real samples.

Table 3 Analysis results of moisture content in real samples

Sample	Detected water content (%)	Recovery (%)	RSD (%)
1	5.15	103	3.0
	4.87	97.4	
	5.08	102	
2	4.79	95.8	2.7
	4.86	97.2	
	5.07	101	
3	5.20	104	3.7
	5.16	103	
	4.85	97	

Conclusions

In summary, we designed a sensitive, simple and rapid method for the determination of water content in ethanol. $CsPbBr_3$@PVA was synthesized and the phase transition from $CsPbBr_3$ to $CsPb_2Br_5$ in PVA was achieved within a few seconds by using ethanol for the first time, during which the fluorescence quenching–recovery process was observed. Importantly, different concentrations of ethanol produce different levels of fluorescence recovery. Based on the above phenomenon, the $CsPbBr_3$@PVA sensor array was prepared by coating the fluorescence-quenched $CsPbBr_3$@PVA on black opaque plastic wafers. The fluorescence images of the sensor treated with an ethanol solution containing different water contents were obtained using a smartphone and analyzed with ImageJ to quickly realize the detection of water content in ethanol. This sensor array shows excellent performance such as a short detection time (only 5 minutes to finish the whole detection process), a relatively wide detection range (0% to 7%) and a very low LOD (0.006%), which are superior to most sensors reported in the literature. Moreover, the sensor array not only displayed outstanding sensitivity, but also realized the water content detection in real samples. Using a smartphone instead of expensive instruments can realize simple, rapid and real-time detection of water content in ethanol in complex environments.

Conflicts of interest

There are no conflicts to declare.

Acknowledgements

This work was financially supported by the National Natural Science Foundation of China with Grant 81927809 and 22004085.

References

1 J. X. Wu and B. Yan, *Dalton Trans.*, 2017, **46**, 7098–7105.
2 M. Z. Zhao, H. Feng, X. X. Zhang, H. Ao and Z. S. Qian, *Analyst*, 2017, **142**, 4613–4617.
3 G. F. Giordano, D. C. M. Ferreira, T. R. de Carvalho, L. C. S. Vieira, M. H. D. Piazzetta, R. S. Lima and A. L. Gobbi, *Anal. Methods*, 2014, **6**, 9497–9502.
4 C. R. Omido, S. L. Oliveira, R. S. Shiraishi, K. F. Magalhaes, V. S. Ferreira, A. A. de Carvalho, C. Kitano and M. H. de Paula, *Sens. Actuators, B*, 2013, **178**, 581–585.
5 K. Fischer, *Angew. Chem.*, 1935, **48**, 394–396.
6 C. A. Barrios, *Sensors*, 2019, **19**, 1–9.
7 M. L. Wang, J. T. Wang and Y. M. Choong, *Food Chem.*, 2004, **86**, 609–615.
8 C. A. Weatherly, R. M. Woods and D. W. Armstrong, *J. Agric. Food Chem.*, 2014, **62**, 1832–1838.

9 P. Yadav and M. C. Bhatnagar, *AIP Conf. Proc.*, 2013, **1512**, 488–489.
10 D. P. De Queiroz, A. De Oliveira Florentino, J. C. Bruno, J. H. D. Da Silva, A. Riul Jr. and J. A. Giacometti, *Sens. Actuators, B*, 2016, **230**, 566–570.
11 S. Kanaparthi, *Flexible Printed Electron.*, 2018, **3**, 015009.
12 S. Castritius, A. Kron, T. Schäfer, M. Rädle and D. Harms, *J. Agric. Food Chem.*, 2010, **58**, 12634–12641.
13 C. L. Sanford, B. A. Mantooth and B. T. Jones, *J. Chem. Educ.*, 2001, **78**, 1221.
14 P. Brereton, S. Hasnip, A. Bertrand, R. Wittkowski and C. Guillou, *Trends Anal. Chem.*, 2003, **22**, 19–25.
15 Y. Ooyama, K. Uenaka, A. Matsugasako, Y. Harima and J. Ohshita, *RSC Adv.*, 2013, **3**, 23255–23263.
16 H. S. Jung, P. Verwils, W. Y. Kim and J. S. Kim, *Chem. Soc. Rev.*, 2016, **45**, 1242–1256.
17 Y. J. Fan, J. W. Li, Y. P. Guo, L. W. Xie and G. Zhang, *Measurement*, 2021, **171**, 108829.
18 H. Q. Wang, L. Yang, S. Y. Chu, B. H. Liu, Q. K. Zhang, L. M. Zou, S. M. Yu and C. L. Jiang, *Anal. Chem.*, 2019, **91**, 9292–9299.
19 D. G. Jiang, Y. F. Tian, Y. J. Zhang, X. Y. Lu, D. Xiao and C. S. Zhou, *Anal. Chim. Acta*, 2021, **1171**, 338645.
20 N. X. Kong, H. Yuan, H. M. Zhou, Y. Zhao and S. J. Zhang, *Anal. Methods*, 2021, **13**, 2722–2727.
21 X. L. Zhang, K. R. Huang, N. L. Zhang, Z. F. Luo, C. Q. Wang, L. B. Xian, F. C. Jiang and X. T. Li, *J. Phys. Chem. Lett.*, 2021, **12**, 11042–11049.
22 Q. V. Le, K. Hong, H. W. Jang and S. Y. Kim, *Adv. Electron. Mater.*, 2018, **4**, 1800335.
23 M. Jung, T. J. Shin, J. Seo, G. Kim and S. I. Seok, *Energy Environ. Sci.*, 2018, **11**, 2188–2197.
24 H. Huang, M. I. Bodnarchuk, S. V. Kershaw, M. V. Kovalenko and A. L. Rogach, *ACS Energy Lett.*, 2017, **2**, 2071–2083.
25 Z. F. Shi, Y. Li, Y. T. Zhang, Y. S. Chen, X. J. Li, D. Wu, T. T. Xu, C. X. Shan and G. T. Du, *Nano Lett.*, 2017, **17**, 313–321.
26 S. L. Mei, X. Y. Liu, W. L. Zhang, R. Liu, L. R. Zheng, R. Q. Guo and P. F. Tian, *ACS Appl. Mater. Interfaces*, 2018, **10**, 5641–5648.
27 X. L. Zhang, H. Liu, W. G. Wang, J. B. Zhang, B. Xu, K. L. Karen, Y. J. Zheng, S. Liu, S. M. Chen, K. Wang and X. W. Sun, *Adv. Mater.*, 2017, **29**, 1606405.
28 C. H. Jiang, J. S. Yao, P. Huang, R. F. Tang, X. M. Wang, X. Y. Lei, H. Zeng, S. Chang, H. Z. Zhong, H. B. Yao, C. F. Zhu and T. Chen, *Cell Rep. Phys. Sci.*, 2020, **1**, 100001.
29 P. Ramasamy, D. H. Lim, B. Kim, S. H. Lee, M. S. Lee and J. S. Lee, *Chem. Commun.*, 2016, **52**, 2067–2070.
30 Y. Li, Q. H. Shu, Q. Du, Y. Dai, S. W. Zhao, J. X. Zhang, L. J. Li and K. Chen, *ACS Appl. Mater. Interfaces*, 2019, **12**, 451–460.
31 L. Ding, B. Borjigin, Y. N. Li, X. X. Yang, X. J. Wang and H. Q. Li, *ACS Appl. Mater. Interfaces*, 2021, **13**, 51161–51173.
32 B. Turedi, K. J. Lee, I. Dursun, B. Alamer, Z. Wu, E. Alarousu, O. F. Mohammed, N. Cho and O. M. Bakr, *J. Phys. Chem. C*, 2018, **122**, 14128–14134.
33 G. Maity and S. K. Pradhan, *J. Alloys Compd.*, 2020, **816**, 152612.
34 M. Liu, J. T. Zhao, Z. L. Luo, Z. H. Sun, N. Pan, H. Y. Ding and X. P. Wang, *Chem. Mater.*, 2018, **30**, 5846–5852.
35 M. Li, X. Zhang, T. Dong, P. Wang, K. M. Postolek and P. Yang, *J. Phys. Chem. C*, 2018, **122**, 28968–28976.
36 K. H. Wang, L. Wu, L. Li, H. B. Yao, H. S. Qian and S. H. Yu, *Angew. Chem.*, 2016, **128**, 8468–8472.
37 X. S. Tang, Z. P. Hu, W. Yuan, W. Hu, H. B. Shao, D. J. Han, J. F. Zheng, J. Y. Hao, Z. G. Zang, J. Du, Y. X. Leng, L. Fang and M. Zhou, *Adv. Opt. Mater.*, 2017, **5**, 1600788.
38 H. Shankar, P. Bansal, W. W. Yu and P. Kar, *Chem. – Eur. J.*, 2020, **26**, 12242–12248.
39 L. S. Rao, X. R. Ding, X. W. Du, G. W. Liang, Y. Tang, K. R. Tang and J. Z. Zhang, *Beilstein J. Nanotechnol.*, 2019, **10**, 666–676.
40 Z. P. Huang, B. Ma, H. Wang, N. Li, R. T. Liu, Z. Q. Zhang, X. D. Zhang, J. H. Zhao, P. Z. Zheng, Q. Wang and H. L. Zhang, *J. Phys. Chem. Lett.*, 2020, **11**, 6007–6015.
41 N. Li, S. G. Liu, Y. Z. Fan, Y. J. Ju, N. Xiao, H. Q. Luo and N. B. Li, *Anal. Chim. Acta*, 2018, **1013**, 63–70.
42 H. Wang, X. Wang, R. Chen, H. Zhang, X. Wang, J. Wang, J. Zhang, L. C. Mu, K. F. Wu, F. T. Fan, X. Zong and C. Li, *ACS Energy Lett.*, 2018, **4**, 40–47.
43 J. Yuan, X. Ling, D. Yang, F. Li, S. Zhou, J. Shi, Y. L. Qian, J. X. Hu, Y. S. Sun, Y. G. Yang, X. Y. Gao, S. Duhm, Q. Zhang and W. Ma, *Joule*, 2018, **2**, 2450–2463.
44 J. M. Frost, K. T. Butler, F. Brivio, C. H. Hendon, M. Van Schilfgaarde and A. Walsh, *Nano Lett.*, 2014, **14**, 2584–2590.
45 B. Akbali, G. Topçu, T. Guner, M. Ozcan, M. M. Demir and H. Sahin, *Phys. Rev. Mater.*, 2018, **2**, 034601.
46 X. S. Tang, S. Han, Z. Q. Zu, W. Hu, D. Zhou, J. Du, Z. P. Hu, S. Q. Li and Z. G. Zang, *Front. Phys.*, 2018, **5**, 69.
47 Y. Q. Dong, J. H. Cai, Q. Q. Fang, X. You and Y. W. Chi, *Anal. Chem.*, 2016, **88**, 1748–1752.
48 X. Y. Sun, L. F. Cai, W. He, X. G. Cao, B. Liu and H. Q. Wang, *Spectrochim. Acta, Part A*, 2022, **264**, 120266.
49 J. Wang, J. Y. Wang, W. X. Xiao, Z. Geng, D. Tan, L. Wei, J. H. Li, L. J. Xue, X. B. Wang and J. T. Zhu, *Anal. Methods*, 2020, **12**, 3218–3224.
50 C. L. Ye, Y. J. Qin, P. C. Huang, A. F. Chen and F. Y. Wu, *Anal. Chim. Acta*, 2018, **1034**, 144–152.
51 X. Y. Wang, C. G. Niu, L. Y. Hu, D. W. Huang, S. Q. Wu, L. Zhang, X. J. Wen and G. M. Zeng, *Sens. Actuators, B*, 2017, **243**, 1046–1056.
52 S. Kanaparthi, *Flexible Printed Electron.*, 2018, **3**, 015009.
53 D. Surangsrirat, V. Sridhar, O. Srikun, M. Puanglamjeak, P. Birdi, S. Dumnin, C. Thanawattano and K. S. Chana, *RSC Adv.*, 2022, **12**, 6181–6185.

